Multi-Scenario Broadband Channel Measurement and Modeling for Sub-6 GHz RIS-Assisted Wireless Communication Systems

Jian Sang, Mingyong Zhou, Jifeng Lan, Boning Gao, Wankai Tang, Xiao Li, Shi Jin, Ertugrul Basar, Cen Li, Qiang Cheng, and Tie Jun Cui

Abstract

Reconfigurable intelligent surface (RIS)-empowered communication, has been considered widely as one of the revolutionary technologies for next generation networks. However, due to the novel propagation characteristics of RISs, underlying RIS channel modeling and measurement research is still in its infancy and not fully investigated. In this paper, we conduct multi-scenario broadband channel measurements and modeling for RIS-assisted communications at the sub-6 GHz band. The measurements are carried out in three scenarios covering outdoor, indoor, and outdoor-to-indoor (O2I) environments, which suffer from non-line-of-sight (NLOS) propagation inherently. Three propagation modes including intelligent reflection with RIS, specular reflection with RIS and the mode without RIS, are taken into account in each scenario. In addition, considering the cascaded characteristics of RIS-assisted channel by nature, two modified empirical models including floating-intercept (FI) and close-in (CI) are proposed, which cover distance and angle domains. The measurement results rooted in 2096 channel acquisitions verify the prediction accuracy of these proposed models. Moreover, the propagation characteristics for RIS-assisted channels, including path loss (PL) gain, PL exponent, spatial consistency, time dispersion, frequency stationarity, etc., are compared and analyzed comprehensively. These channel measurement and modeling results may lay the groundwork for future applications of RIS-assisted communication systems in practice.

Jian Sang, Mingyong Zhou, Jifeng Lan, Boning Gao, Wankai Tang, Xiao Li, and Shi Jin are with the National Mobile Communications Research Laboratory, Southeast University, Nanjing 210012, China.

Ertugrul Basar is with the Communications Research and Innovation Laboratory (CoreLab), Department of Electrical and Electronics Engineering, Koç University, Sariyer, Istanbul 34450, Turkey.

Cen Li is with the China Communications Technology Co., Ltd, Nanjing 210012, China.

Qiang Cheng, and Tie Jun Cui are with the State Key Laboratory of Millimeter Waves, Southeast University, Nanjing 210012, China.

Index Terms

RIS-assisted systems, channel measurement, channel modeling, sub-6 GHz.

I. Introduction

With the deployment of the fifth generation (5G) communication networks around the world since 2019, the global mobile data traffic has experienced a dramatic growth, which is anticipated to reach 5016 exabytes per month (Eb/mo) in 2030 [1]. The evolutionary and advanced sixth generation (6G) communication networks with the even higher requirements, have aroused a surge of interest from both academia and industry nowadays. By 6G networks, many emerging application services such as virtual reality, holographic telepresence, pervasive connectivity, etc., are envisioned promisingly to be realized [2], [3]. Up to now, although no detailed specifications have been laid out on the communication standard of 6G, the study of possible innovating technologies, applicable propagation model and practical channel measurement facing 6G, have been the focus of initiatives in various countries [4], [5].

Reconfigurable intelligent surface (RIS)-empowered communication, with its ability of controlling the propagation environment effectively, has recently been considered one of the revolutionary technologies to meet the ever-increasing 6G demands [6], [7]. RIS provides a prospective concept by manipulating the electromagnetic (EM) wave which is impinging on it and reflected to the desired direction, with a relatively low power consumption. By this means, RIS can constructively customize wireless channels instead of traditionally adapting to the harsh propagation environment [8].

Generally speaking, an RIS is composed of an artificial meta-surface with plentiful sub-wavelength sized unit cells arranged in an array form. The reflection coefficients of each unit cell, e.g., magnitude, phase, polarization, etc., can be reconfigured intelligently through adjusting the control voltage [9]. Typically, each unit cell is comprised of conductive printed patch, which has a size of proportion to the wavelength of operating frequency. In order to reconfigure the EM response, a tunable load, such as positive-intrinsic-negative (PIN) diode or varactor diode, could be embedded into unit cell to interact with control voltage. In this way, the EM characteristics of the outgoing signal can be programmed independently by a smart controller such as field programmable gate array (FPGA) in real time. Thanks to such innovative characteristics brought by RISs, the radio propagation environment may be redefined [10], [11].

Until now, numerous analyses on RIS-empowered systems have been theoretically investigated in many fields, including but not limited to: user localization [12], secure communication [13], beam optimization [14], user scheduling [15], etc. Meanwhile, theoretical channel modeling as well as practical measurements, on power gain and coverage enhancement of RIS-assisted non-line-of-sight (NLOS) communications have gradually been reported [16], [17]. Nevertheless, the real channel measurement campaign and applicable channel model in practice, which describe the underlying physical propagation phenomena of EM waves incurred by RIS, are still in their infancy and rarely proposed, despite their critical roles.

A. Modeling-related works

Considering broadcast and beamforming scenarios respectively, [18] and [19] theoretically formulated the path loss (PL) expressions for RIS-assisted NLOS communications in free space. Then a two-path propagation model for RIS-assisted communications was proposed in [20], which showed that the deployment of RIS was advantageous for mitigating fast fading. In [21], a physics-driven PL model for RIS-assisted link in free space was proposed based on antenna theory. In [22], the PL scaling law of the scattered field was discussed numerically, which unified the opposite behavior of RIS serving as a scatterer and a mirror. [23] formulated the RIS-related PL models by using the vector generalization of Green's theorem. In [24], a PL model for RIS-assisted systems was proposed based on physical optics technique, which explained the mechanism why the plentiful unit cells on RIS individually acted as diffuse scatterers but could jointly perform beamforming in a desired direction. [25] considered that RIS were partitioned into several tiles, which yielded the free-space tile response model for RIS-assisted link. In [26], an RIS channel simulator was introduced by considering the 3GPP channel modeling methodology for millimeter wave (mmWave) channels.

B. Measurement-related works

In [18], Tang *et al.* conducted the measurements to validate PL models in an anechoic chamber, utilizing three RISs at 4.25 GHz and 10.5 GHz respectively. Further mmWave measurements on two customized RIS covering 27 GHz and 33 GHz were carried out in [19] to verify the refined PL models. In [27], two RISs constituted of varactor diodes and PIN diodes respectively, were employed in an indoor environment to illustrate the RIS-related channel reciprocity. By utilizing universal software radio peripherals (USRPs), the measurement campaigns in [28] illustrated

that an RIS could bring a power gain of 27 dB and 14 dB for short-range and long-range communications, respectively. In [29], a signal-to-noise ratio (SNR) gain of 8 dB was shown to be offered by the RIS at 5.8 GHz when the NLOS distance reached 35 m. [30] proposed a spectrum sharing solution using RIS in indoor channel, where experiments conducted at 2.4 GHz demonstrated a higher spectrum-spatial efficiency by controlling the phase shifts of RIS. A 1-bit RIS fabricated in [31] validated its capability of enhancing power gains by conducting the indoor measurements at 3.5 GHz. In [32], the experiments conducted on a multi-bit RIS substantiated a power improvement of 2.65 dB compared with 1-bit RIS. In [33], the RIS experiments at 28 GHz manifested its capability for transmission signal enhancement in NLOS links. Considering the RIS serving as transmitter (Tx), the measurements at 28 GHz in [34] illustrated that the PL in the main beam directions were improved by RIS. [35] considered practical measurements at 5 GHz and employed RIS codebooks to dynamically adjust the RIS phases depending on user locations. In terms of physical layer security, measurements were performed in [36], which showed that with RIS deployment, the signal level of an eveasdropper could be reduced down to the noise floor.

Though the above-mentioned studies have largely developed RIS-based free-space models and power-related measurements, unabridged channel observations in practical environment are still rarely reported. Meanwhile, accurate, realistic, yet easy-to-use RIS-empowered channel models are eagar to be developed. Undoubtedly, the RIS-assisted cascaded channel exhibits many new propagation characteristics, such as multi-dimensional PL, diversified propagation modes, unpredictable spatial evolution, etc., which greatly differ from the traditional propagation channels. In consequence, unlike only considering the power gain or simplistically verifying the free-space PL model in existing works, generalizable channel modeling and real channel measurement in practical RIS-related communication scenarios are desired to be fully investigated.

C. Main contributions

Motivated by such circumstances, in this paper, we conduct multi-scenario broadband channel measurements and channel modeling for RIS-assisted single-input single-output (SISO) communications. Considering the dominating role of the sub-6 GHz band serving as the 5G commercial operating frequency band [37], the assessment of RIS-assisted channel at this band will probably be of great significance for its future applications, because of the interoperability between RIS and 5G networks. Thus, we carry out the RIS-assisted channel measurements at the sub-6 GHz

licensed frequency band. From multiple perspectives covering frequency domain, spatial domain, and temporal domain, we investigate the propagation characteristics of RIS-assisted channels and explain their underlying phenomena. The major contributions are listed as follows.

- We conduct broadband channel measurement campaigns at 2.6 GHz for RIS-assisted NLOS propagation in three scenarios, covering outdoor, indoor, and outdoor-to-indoor (O2I) measurements. Three propagation modes including intelligent reflection with RIS, specular reflection with RIS, and the mode without RIS, are considered in each scenario. In addition, the measured channel data is also compared with the free-space propagation model. The multi-dimensional parameters including Tx-RIS distance, receiver (Rx)-RIS distance, angle-of-arrival (AoA) onto RIS, and angle-of-departure (AoD) from RIS, etc., are taken into account in our measurement.
- We propose the modified empirical floating-intercept (FI) and close-in (CI) models, to cater for the multi-parameter characteristics of RIS-assisted channels. In comparison to the CI and FI models that we previously proposed in [38], we further refine them from single-dimensional variable to multi-dimensional variables, with distance information as well as angle information included.
- The measurement results are presented and the modeling accuracy is analyzed. From multiple perspectives covering PL gain, PL exponent (PLE), spatial consistency, time dispersion, frequency stationarity, etc., we investigate the characteristics of RIS-assisted channels under different modes as well as in different scenarios. Their underlying propagation phenomena such as the claim of "customizing wireless channels", are explained and several potential research directions are also pointed out.

D. Organization

The remainder of this paper is outlined as follows. In Section II, the measurement systems and the deployed RIS are described in detail. The measurement scenarios and the measurement procedures are provided in Section III. Then the post-processing of measurement data and the proposed channel models are illustrated in Section IV. In Section V, the measurement results and modeling analyses are presented. Finally, conclusions are drawn and several future works are laid out in Section VI.

II. Channel Measurement Systems and the Deployed RIS

In this paper, an RIS-assisted SISO communication system is considered, as shown in Fig. 1. The direct channel between Tx and Rx is blocked by obstacles, i.e., a NLOS channel. An RIS is deployed to assist the signal propagation, which is referred to the RIS-assisted channel with cascaded LOS link in the rest of this paper. The RIS consists of M unit cells per row and N unit cells per column, i.e., $M \times N$ unit cells in total. Each unit cell has a rectangular shape with a horizontal size of d_x and a vertical size of d_y. Moreover, each unit cell has a constant reflection magnitude A and programmable binary discrete phases. Note that the RIS in this paper refers to the family of reflective RIS, by which the signal is neither amplified nor retransmitted. As shown in Fig. 1, let d_1 and d_2 refer to the distances from Tx to the center of RIS and from Rx to the center of RIS, respectively. θ_t, φ_t, θ_r and φ_r respectively indicate the elevation angle-of-arrival (EAoA) and the azimuth angle-of-arrival (AAoA) onto RIS as well as the elevation angle-of-departure (EAoD) and the azimuth angle-of-departure (AAoD) from RIS.

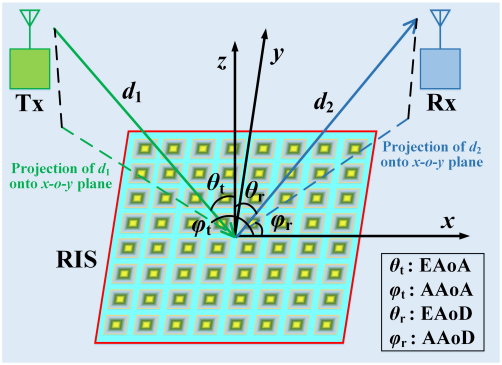


Fig. 1. Parameter definitions for RIS-assisted channel.

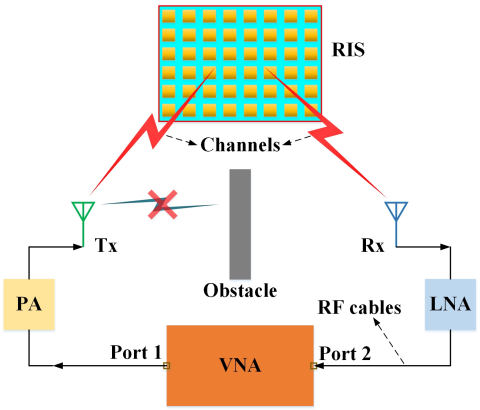


Fig. 2. Descriptions of channel measurement systems.

A. Channel measurement systems

As shown in Fig. 2, the channel measurement systems are composed of a VNA, a fabricated RIS, a power amplifier (PA), a low noise amplifier (LNA), radio frequency (RF) cables, and two directional horn antennas. In detail, the used VNA version is Agilent N5230C PNA-L. The bandwidth of 190 MHz ranging from 2.5 GHz to 2.69 GHz is selected for the measured broadband signal, which covers the licensed frequency band of current commercial mobile networks [37]. There are 191 scanning points within this measurement bandwidth, with scanning time of 27.3 μs for each point by the VNA. As shown in Fig. 2, the port 1 of VNA is used to transmit signal and its port 2 receives the signal. Therefore, the scanning data S_{21} is collected as channel transfer function (CTF) in frequency domain. In addition, the antennas used in the measurement system

are two wideband double-ridged horn antennas, which serve as Tx and Rx respectively. Each of them is vertically polarized with a gain of 8.25 dBi and has a half power beam width (HPBW) of 60 degrees. The PA connected to Tx has a 30 dB gain and the LNA connected to Rx has a 24 dB gain. The low-loss RF cables with stable amplitude and phase responses are utilized to connect the above equipment. The detailed configurations and parameters of the measurement systems are summarized in Table I.

TABLE I

CONFIGURATIONS AND PARAMETERS OF MEASUREMENT SYSTEMS.

Configuration	**Parameter**	**Configuration**	**Parameter**
Measurement bandwidth	190 MHz, $2.5 \sim 2.69$ GHz	Transmitted power of VNA	10 dBm
Number of frequency scanning points	191	Antenna gain of Tx/Rx	8.25 dBi
Scanning time for one measurement	0.0273 ms$\times$ $191 \approx 5.21$ ms	Antenna HPBW of Tx/Rx	60°
Antenna polarization of Tx/Rx	vertical	Loss of RF cables	≤ 0.5 dB/m
PA gain	30 dBm	LNA gain	24 dBm
Size of RIS	1.6 m $\times$ 0.8 m	Number of unit cell	$32 \times 16 = 512$
Size of unit cell	0.05 m $\times$ 0.05 m	Phase resolution of unit cell	1-bit
Phase levels of unit cell	$\{$ 55° for coding "0", -125° for coding "1"$\}$	Phase difference of unit cell	180°

B. The deployed RIS

As displayed in Fig. 3, a fabricated RIS with the central operating frequency of 2.6 GHz is utilized for channel measurements. This RIS is composed of 32 unit cells per column and 16 unit cells per row, i.e., 512 unit cells in total, which has a physical size of 1.6 m $\times$ 0.8 m. Each unit cell on the RIS has a square shape of 0.05 m $\times$ 0.05 m, which is nearly half-wavelength of the central operating frequency. A PIN diode is embedded into the unit cell to tune the response characteristics of impinging EM waves. In addition, each unit cell can be independently programmed with 1-bit phase resolution, i.e., two coding states of coding "0" and coding "1", which correspond to the PIN diode being "off" state and "on" state, respectively.

Fig. 3 also shows the magnitude and phase response curves of this RIS with respect to the operating frequency. Within the measurement bandwidth from 2.5 GHz to 2.69 GHz, the magnitude has an average loss of 0.25 dB for coding "1" and an average loss of 0.75 dB for coding "0", respectively. It is worth mentioning that these losses are much lower than the gain to be provided by RIS beamforming. In addition, within the measurement bandwidth, the phase has an average value of 55° for coding "1" and an average value of -125° for coding "0". Thus, a phase difference of 180° between these two coding states can be achieved.

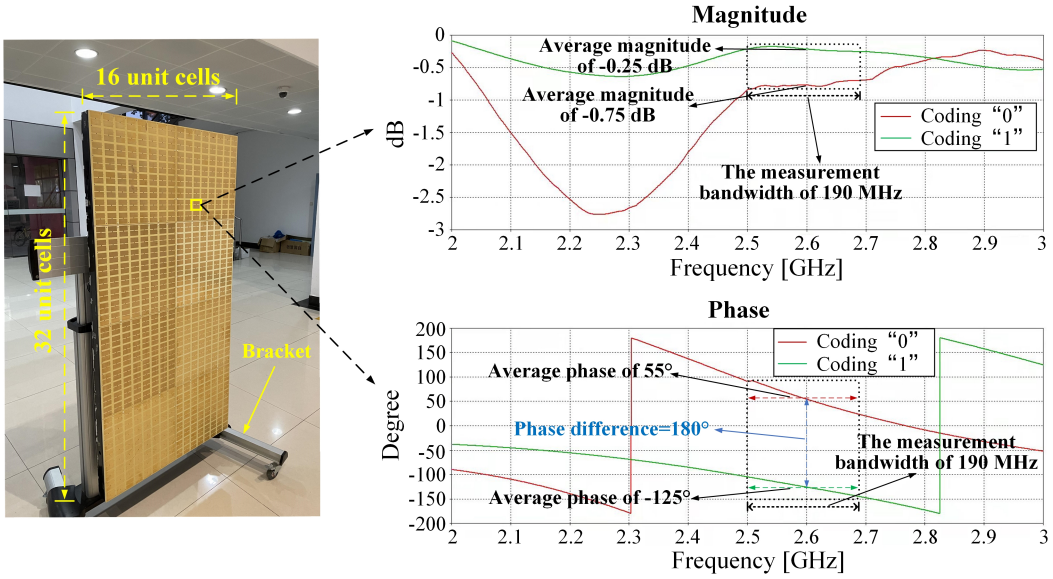


Fig. 3. Image and response characteristics of the deployed RIS.

By pre-designing the coding of each unit cell, this RIS can perform arbitrary beamforming towards desired azimuth and elevation directions. Note that in this paper, the coding schemes of RIS are designed by **"Dynamic Threshold Phase Quantization (DTPQ) method"** in [39], which can be regarded as the optimal scheme in free space and applicable to various communication scenarios. In our measurement campaigns, firstly the parameters d_1, d_2, θ_t, φ_t, θ_r and φ_r of the RIS-assisted channels at each point are measured and calculated respectively, according to the geometric position. Based on these parameters, we utilize the "DTPQ method" to generate the codebooks of RIS, which are mapped to each measured point one-to-one. Then, the channel data at each measured point is collected with RIS configuring the corresponding codebook.

III. Channel Measurement Scenarios and Procedures

In order to comprehensively investigate the propagation characteristics of RIS-assisted channel in practical communications, three typical scenarios including outdoor, indoor, and O2I environments are selected to conduct channel measurement, which cover 2096 channel acquisitions to be measured in total. These measurement scenarios are located at Jiulonghu Campus of Southeast University, in Nanjing, China. The images of channel measurement campaigns in these scenarios are respectively exhibited in Fig. 4. Our measurement campaigns are conducted at night so as to avoid the influences of pedestrians or vehicles on the measurement results. Thus, the measured channels can be viewed as quasi-static. In particular, the detailed information on measurement scenarios and procedures are provided in the subsequent subsections.

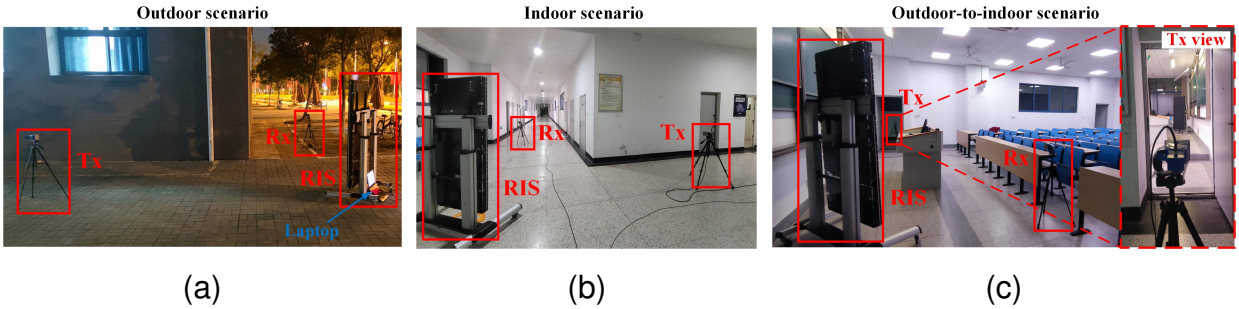


Fig. 4. Images of three channel measurement campaigns. (a) Outdoor scenario. (b) Indoor scenario. (c) O2I scenario.

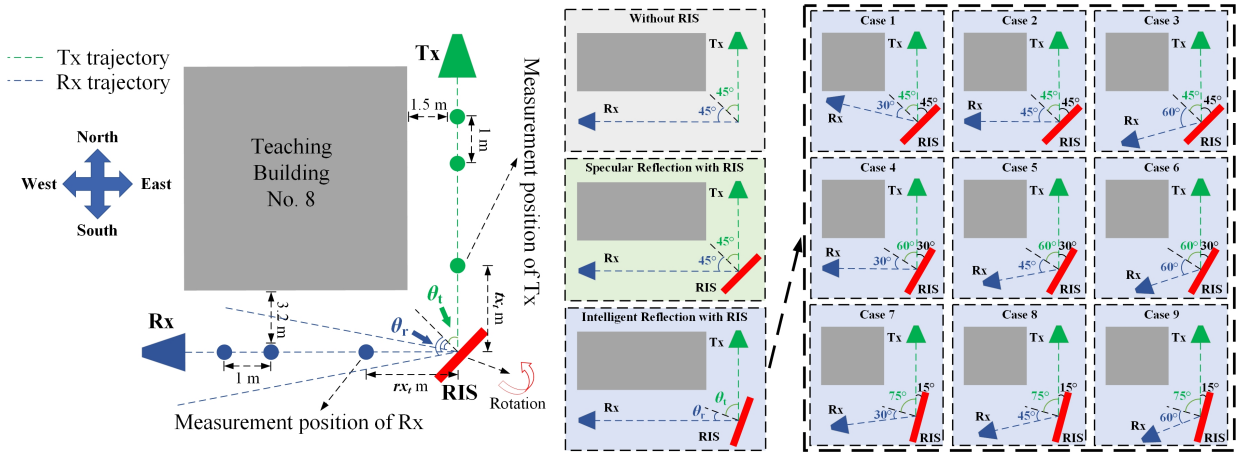


Fig. 5. Scenario and procedure for outdoor measurement.

A. *Outdoor channel measurement*

For outdoor measurement, the building corner next to Teaching Building No. 8 outdoors is selected as measurement site. The scenario and procedure for this measurement are exhibited in Fig. 5. As shown in this figure, the communication links between two sides of this building suffer from NLOS propagation, due to the blockage by the exterior wall of building. The exterior facades of this building are fully covered by concretes. Two horn antennas serving as Tx and Rx, are respectively placed at the east-side and south-side spaces of the building.

From Fig. 5, Tx is kept at a perpendicular distance of 1.5 m from the east facades of building, and moves along the line (referred to as "Tx trajectory line") parallel to the east facades. In addition, Rx is kept at a perpendicular distance of 3.2 m from the south facades of building, and moves along the line (referred to as "Rx trajectory line") parallel to the south facades. The RIS is positioned at the intersection of Tx and Rx trajectory lines. Throughout this measurement, both Tx and Rx maintain facing the RIS.

Tx is initially placed at a distance of tx_t m from RIS and moves away from RIS at a step of 1 m along the Tx trajectory line, until the Tx-RIS distance reaches tx_p m. Similarly, Rx is initially

placed at a distance of rx_t m from the RIS and moves away from RIS at a step of 1 m along the Rx trajectory line, until the Rx-RIS distance reaches rx_p m. Note that in this measurement, Tx, Rx, and the center of RIS are fixed to be at the same height of 1 m above the ground, thus the AAoA $\varphi_t = 180^\circ$ and the AAoD $\varphi_r = 0^\circ$ invariably.

TABLE II

MEASUREMENT PARAMETERS OF OUTDOOR SCENARIO.

Propagation mode	**Without RIS**	**Specular reflection with RIS**	**Intelligent reflection with RIS**								
			Case 1	Case 2	Case 3	Case 4	Case 5	Case 6	Case 7	Case 8	Case 9
EAoA θ_t	45° *(virtual)*	45°	45°	45°	45°	60°	60°	60°	75°	75°	75°
EAoD θ_r	45° *(virtual)*	45°	30°	45°	60°	30°	45°	60°	30°	45°	60°
tx_t (m)	5	5	9	5	9	9	9	9	9	9	9
tx_p (m)	18	18	18	18	18	18	18	18	18	18	18
rx_t (m)	5	5	5	5	8	8	8	8	8	8	8
rx_p (m)	18	18	12	18	15	18	15	15	15	15	15
Number of Tx points	14	14	10	14	10	10	10	10	10	10	10
Number of Rx points	14	14	8	14	8	11	8	8	8	8	8
Number of total points	$14 \times 14 = 196$	$14 \times 14 = 196$	$10 \times 8 + 14 \times 14 + 10 \times 8 + 10 \times 11 + 10 \times 8 + 10 \times 8 + 10 \times 8 + 10 \times 8 + 10 \times 8 = 866$								

In this measurement, the channels under three propagation modes are measured, including *specular reflection with RIS*, *intelligent reflection with RIS*, and *without RIS*. These three modes include 196, 866, and 196 points to be measured respectively. The detailed configurations on these three modes are parameterized in Table II, which are illuminated as follows.

For the mode of specular reflection with RIS, the RIS is fixed at $\theta_t = 45^\circ$ and $\theta_r = 45^\circ$. tx_t, tx_p, rx_t, and rx_p are 5 m, 18 m, 5 m, and 18 m, respectively. In this mode, the RIS does not perform phase regulation, and all unit cells of RIS are uniformly configured to be coding "0". Thus, the RIS can be regarded to be equivalent to an equal-sized metal plate [19].

For the mode of intelligent reflection with RIS, the RIS performs phase regulation according to the coding scheme mentioned in Section II-B. In this mode, RIS is appropriately rotated to form 9 different pairs of EAoA θ_t and EAoD θ_r, i.e., $\theta_t \in \{45^\circ, 60^\circ, 75^\circ\}$ and $\theta_r \in \{30^\circ, 45^\circ, 60^\circ\}$, as illustrated in Fig. 5.

For the mode without RIS, the RIS is removed. Thus, there are a virtual EAoA $\theta_t = 45^\circ$ and a virtual EAoD $\theta_r = 45^\circ$. tx_t, tx_p, rx_t, and rx_p are 5 m, 18 m, 5 m, and 18 m, respectively.

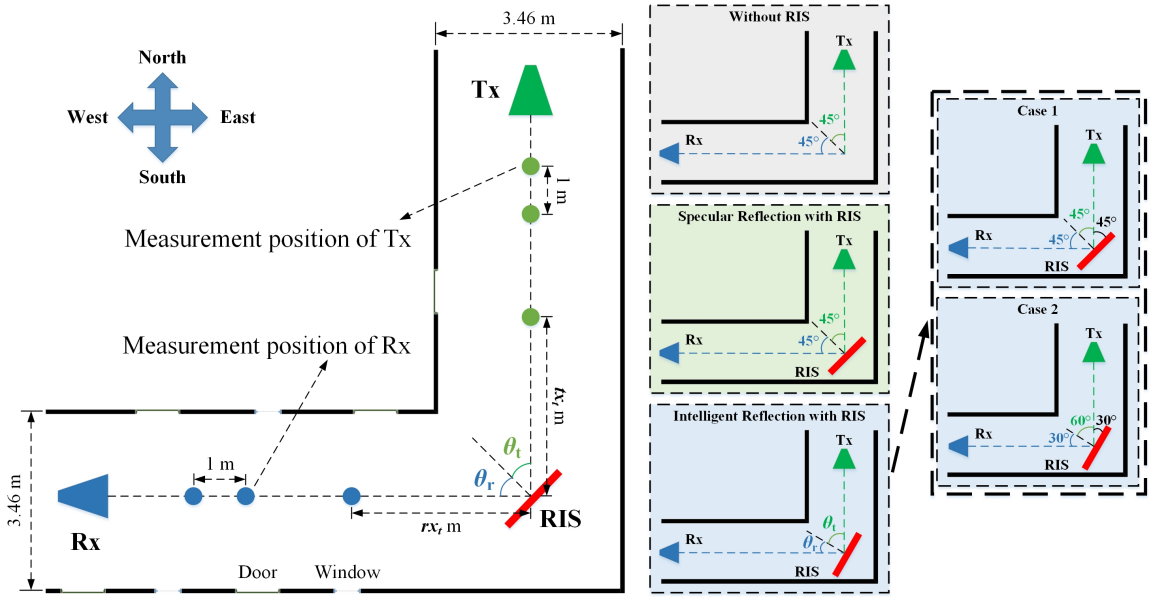


Fig. 6. Scenario and procedure for indoor measurement.

B. Indoor channel measurement

For indoor measurement, the corridor on the first floor of Teaching Building No. 2, which is next to the Liangjiang Road, is selected as measurement site. The measurement scenario and procedure are shown in Fig. 6. From this figure, an inherent NLOS transmission link exists, due to the fact that both sides of the corridor are perpendicular to each other. The walls of this corridor are covered with concrete, among which the aluminum alloy doors and several glazed windows are embedded. The corridor has a width of 3.46 m and a height of 3.32 m. The south-north corridor and the east-west corridor are respectively selected to place Tx and Rx, and the RIS is employed at the corner of corridor. Two horn antennas serving as Tx and Rx are respectively placed facing the RIS throughout this measurement.

As shown in Fig. 6, Tx moves along the central axis of south-north corridor (referred to as "Tx trajectory line") and Rx moves along the central axis of east-west corridor (referred to as "Rx trajectory line"). The RIS is positioned at the intersection of Tx and Rx trajectory lines. Tx is initially placed at a distance of tx_t m from RIS and moves away from RIS at a step of 1 m along the Tx trajectory line, until the Tx-RIS distance reaches tx_p m. Similar with the outdoor scenario, Rx is initially placed at a distance of rx_t m from the RIS and moves away from RIS at a step of 1 m along the Rx trajectory line, until the Rx-RIS distance reaches rx_p m. In this measurement, Tx, Rx, and the center of RIS are also fixed to be at the same height of 1 m above the ground, thus the AAoA $\theta_t = 180°$ and the AAoD $\theta_r = 0°$ invariably.

In this measurement, three propagation modes as in the outdoor scenario, including *specular reflection with RIS*, *intelligent reflection with RIS*, and *without RIS*, are also measured. These three modes contain 196, 392, and 196 points to be measured respectively. The detailed configurations of the three modes are summarized in Table III, which are further illuminated as follows.

TABLE III

MEASUREMENT PARAMETERS OF INDOOR SCENARIO.

Propagation mode	**Without RIS**	**Specular reflection with RIS**	**Intelligent reflection with RIS**	
			Case 1	Case 2
EAoA θ_t	45° *(virtual)*	45°	45°	60°
EAoD θ_r	45° *(virtual)*	45°	45°	30°
tx_t (m)	5	5	5	5
tx_p (m)	18	18	18	18
rx_t (m)	5	5	5	5
rx_p (m)	18	18	18	18
Number of Tx points	14	14	14	14
Number of Rx points	14	14	14	14
Number of total points	$14 \times 14 = 196$	$14 \times 14 = 196$	$14 \times 14 + 14 \times 14 = 392$	

For the mode of specular reflection with RIS, the RIS is fixed at $\theta_t = 45^\circ$ and $\theta_r = 45^\circ$. Meanwhile, tx_t, tx_p, rx_t, and rx_p are 5 m, 18 m, 5 m, and 18 m, respectively. In this mode, the RIS does not perform phase regulation and all unit cells of RIS are uniformly configured to be coding "0". For the mode of intelligent reflection with RIS, the RIS performs phase regulation according to the coding scheme mentioned in Section II-B. In this mode, RIS is appropriately rotated to form 2 different pairs of θ_t and θ_r, i.e., $\theta_t = 45^\circ$, $\theta_r = 45^\circ$ and $\theta_t = 60^\circ$, $\theta_r = 30^\circ$, as illustrated in Fig. 6. For the mode without RIS, measurement settings are the same with the corresponding mode in the outdoor scenario, as shown in Table III.

C. O2I channel measurement

For O2I measurement, the classroom on the first floor of Teaching Building No. 7, is selected as measurement site. The scenario and procedure for this measurement are exhibited in Fig. 7. In this scenario, Rx in the classroom is weakly covered by communication signals when Tx locates outside the classroom, due to the blockage by concrete walls between Tx and Rx. Thus, their communication links can be reasonably considered as NLOS. This measured classroom has a width of 8.26 m, a length of 11.82 m, and a height of 3.32 m. It is surrounded by concrete walls, where several glazed windows and two aluminum alloy doors are embedded into the walls. In

addition, this classroom is typically filled with a number of orderly-arranged desks and chairs, as well as a teacher's table. There are two aisles in the classroom, as shown in Fig. 7.

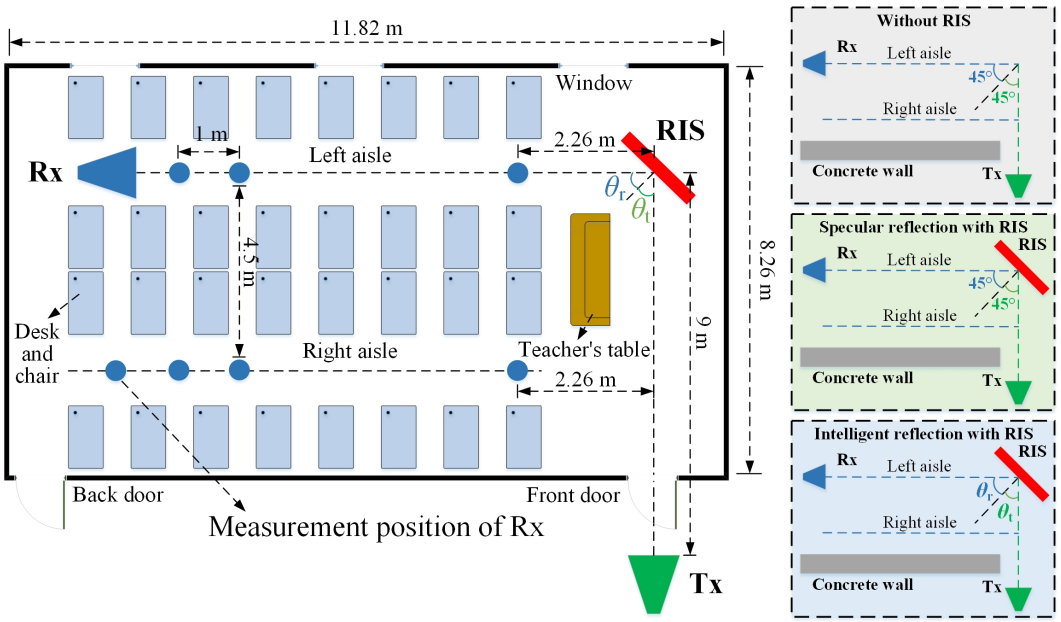


Fig. 7. Scenario and procedure for O2I measurement.

In this measurement, Tx is fixed outside the classroom and faces the front door, which is kept open all along. The RIS is positioned at the intersection of the Tx-front door line and the left aisle, with a distance of 9 m away from Tx and $\theta_t = 45°$. Two horn antennas serving as Tx and Rx maintain facing the RIS throughout this measurement. Rx moves along these two aisles, respectively. In left aisle, $\theta_r = 45°$ can be readily determined at each measured point. Rx is initially placed at a distance of $rx_t = 2.26$ m from RIS and moves away from RIS at a step of 1 m, until the final distance reaches $rx_p = 10.26$ m. In right aisle, Rx is initially positioned at a perpendicular distance of $rx_t = 2.26$ m to the Tx-RIS line, and moves away from this line at a step of 1 m, until the final distance reaches $rx_p = 10.26$ m. Based on geometric position relationships, the EAoD θ_r^i at the ith point in right aisle can be expressed as

$$\theta_r^i = \arctan\left(\frac{2.26 + (i-1) \times 1}{4.5}\right) - \left(\frac{\pi}{2} - \theta_t\right). \tag{1}$$

Then we obtain the EAoD set $\mathcal{R} = \{-18.33°, -9.08°, -1.57°, 4.45°, 9.29°, 13.2°, 16.42°, 19.08°, 21.32°\}$ in the order of positions 1∼9 in right aisle. Similar with the outdoor and indoor scenarios, in this measurement, Tx, Rx, and the center of RIS are also fixed to be at the same height of 1 m above the ground, thus the AAoA $\varphi_t = 180°$ and the AAoD $\varphi_t = 0°$ invariably.

In this measurement, the previously mentioned three propagation modes, i.e., *specular reflection with RIS*, *intelligent reflection with RIS*, and *without RIS*, are measured. The detailed

TABLE IV

MEASUREMENT PARAMETERS OF O2I SCENARIO.

Propagation mode	**Without RIS**		**Specular reflection with RIS**		**Intelligent reflection with RIS**	
	Left aisle	Right aisle	Left aisle	Right aisle	Left aisle	Right aisle
EAoA θ_t	45° *(virtual)*	45° *(virtual)*	45°	45°	45°	45°
EAoD θ_r	45° *(virtual)*	$\mathcal{R}$ *(virtual)*	45°	$\mathcal{R}$	45°	$\mathcal{R}$
d_1 (m)	9	9	9	9	9	9
rx_t (m)	2.26	2.26 (perpendicular distance to Tx-RIS line)	2.26	2.26 (perpendicular distance to Tx-RIS line)	2.26	2.26 (perpendicular distance to Tx-RIS line)
rx_p (m)	10.26	10.26 (perpendicular distance to Tx-RIS line)	10.26	10.26 (perpendicular distance to Tx-RIS line)	10.26	10.26 (perpendicular distance to Tx-RIS line)
Number of Rx points	9	9	9	9	9	9
Number of total points	$9+9=18$		$9+9=18$		$9+9=18$	

configurations on these three modes are summarized in Table IV. The coding schemes of RIS under each mode are the same as the corresponding ones in the outdoor and indoor scenarios. For each mode in this measurement, 18 points are measured.

IV. DATA POST-PROCESSING AND CHANNEL MODELING

In this section, the post-processing of measurement data including PL, PDP, root mean square delay spread (RMS DS), etc., are introduced. In addition, based on the traditionally-used FI and CI models, two empirical channel models for RIS-assisted channel covering distance information and angle information are proposed.

A. Measurement data post-processing

For the sake of illustration, the signals transmitted from port 1 of VNA and received at port 2 of VNA in frequency domain are denoted as $X(f)$ and $Y(f)$ respectively. The measured system response and channel response are represented as $G(f)$ and $H(f)$, respectively. Denote the collected data by VNA as $H_V(f)$, which can be calculated by

$$H_V(f) = S_{21}(f) = \frac{Y(f)}{X(f)} = G(f)H(f). \tag{2}$$

Through the back-to-back calibration, the system response $G(f)$ can be obtained and removed from $S_{21}(f)$. Then the channel response in frequency domain can be calculated by

$$H(f) = \frac{H_V(f)}{G(f)}. \tag{3}$$

The PL of the measured channel in logarithmic scale can be calculated by

$$PL = 10 \times \log_{10}\left(\frac{\sum_{k=1}^{K}\left(|H_k(f)|^2\right)}{K}\right) - G_t - G_r, \tag{4}$$

where $H_k(f)$ denotes the channel response of the kth frequency scanning point, $K = 191$ is the number of frequency scanning points, G_t and G_r denote the antenna gains of Tx and Rx in logarithmic scale, respectively.

Subsequently, the channel impulse response (CIR) in temporal domain can be determined by inverse Fourier transform,

$$h(t,\tau) = \mathrm{IFT}\left(H(f) \times \mathrm{W}_{\mathrm{hann}}\right), \tag{5}$$

where $\mathrm{IFT}(\cdot)$ denotes the inverse Fourier transform operation, $\mathrm{W}_{\mathrm{hann}}$ represents the Hanning-window. Then, the power delay profile (PDP) is calculated by

$$PDP = |h(t,\tau)|^2. \tag{6}$$

In this paper, the multi-path components (MPCs) of PDP above the detection threshold P_{th} are considered valid, and otherwise the MPCs are deemed outliers and discarded. The detection threshold P_{th} can be determined by (7) [40].

$$P_{th} = \max(P_{\max} - \gamma_P, N_0 + \gamma_N), \tag{7}$$

where $P_{\max}$ is the maximum peak power of PDP, γ_P is the power threshold relative to the maximum peak, N_0 is the noise floor of PDP, γ_N is the power threshold relative to the noise floor. In this paper, γ_P and γ_N are set to 60 dB and 15 dB, respectively.

For describing the channel shape in temporal domain, RMS DS can be represented as

$$\tau_{\mathrm{RMS}} = \sqrt{\frac{\sum_{l=1}^{L} P_l {\tau_l}^2}{\sum_{l=1}^{L} P_l} - \left(\frac{\sum_{l=1}^{L} P_l \tau_l}{\sum_{l=1}^{L} P_l}\right)^2}, \tag{8}$$

where L is the number of the valid MPCs in PDP, τ_l denotes the delay of the lth valid MPC calculated by $\tau_l = (l-1)\Delta_\tau$, Δ_τ denotes the delay resolution equaling to the inverse of the measured signal bandwidth, and P_l denotes the power of the lth valid MPC.

B. Channel modeling

In this subsection, the modeling methods for RIS-assisted channels are investigated. In the existing channel-related work, the FI model has been adopted widely to describe the characteristics of PL in the 3rd Generation Partnership Project (3GPP) and International Telecommunication Union (ITU) standards [41], [42]. Meanwhile, though the CI model only focuses on the PLE, it still attracts great attention due to its model parameter stability and intuitive perspective. In [38], we have proposed the applicable FI and CI models to RIS-assisted channel. Nevertheless, these two models in [38] only considered the single-dimensional variable, i.e., the Rx-RIS distance, which limited their generalizations applied in various scenarios. Thus, in this paper, we further refine them from single-dimensional variable to multi-dimensional variables. The modified FI and CI models are proposed for general RIS-assisted channels, which include distance information and angle information.

For the convenience of presentation, the traditional FI model is provided as follows.

$$PL_{FI} = \alpha + 10\beta \log_{10}(d) + X_{\sigma}^{FI}, \tag{9}$$

where d (m) is the three-dimensional (3D) direct distance between Tx and Rx, β is the PLE associated with the variation of distance, α is intercept parameter associated with the offset value of PL, X_{σ}^{FI} is shadow factor (SF) for describing the fitting deviation, which is usually modeled as Gaussian distribution $\mathcal{N}(\mu, \sigma^2)$ [40].

The traditional CI model can be expressed as

$$PL_{CI} = PL_{FS}(d_0) + 10n \log_{10}\left(\frac{d}{d_0}\right) + X_{\sigma}^{CI}, \tag{10}$$

where n is the PLE associated with the variation of distance d, d_0 is the reference distance, which is usually set to 1 m, $PL_{FS}(d_0)$ is the PL at reference distance d_0 in free space, and X_{σ}^{CI} is SF following Gaussian distribution $\mathcal{N}(\mu, \sigma^2)$.

As we can see, both of the traditional FI and CI models focus on the PL fittings under one-dimensional variable (i.e., d). However, for RIS-assisted channel, there are multi-dimensional variables, e.g., d_1, d_2, θ_t, θ_r, etc., to be involved in channel modeling. The theoretical RIS-assisted channel models in free space were proposed in [19], which can be expressed as

$$PL_{FS}^{RIS} = \frac{16\pi^2 (d_1 d_2)^2}{G_t G_r (MN d_x d_y)^2 \cos(\theta_t)\cos(\theta_r) A^2}, \tag{11}$$

where $\cos(\theta_t)$ and $\cos(\theta_r)$ denote the normalized power radiation patterns of emission and reception for unit cell on RIS [19]. From this equation, it can be readily derived that, in free

space, the PLEs on d_1 and d_2 are 2 and the PLEs on $\cos(\theta_t)$ and $\cos(\theta_r)$ are 1 in logarithmic scale, respectively. As a consequence, the traditional FI and CI models should be deformed to adapt to multi-dimensional variables of RIS-assisted channel.

In this paper, we propose the modified FI and CI models for the PL of RIS-assisted channel, as expressed in (12) and (13) respectively.

$$\begin{aligned} PL_{FI}^{RIS}\left(d_1,d_2,\theta_t,\theta_r\right) =& \alpha + 10\beta_1 \log_{10}\left(d_1\right) + 10\beta_2 \log_{10}\left(d_2\right) - 10\lambda_1 \log_{10}\left(\cos\left(\theta_t\right)\right) \\ & - 10\lambda_2 \log_{10}\left(\cos\left(\theta_r\right)\right) + X_{\sigma}^{FI}, \end{aligned} \tag{12}$$

where β_1 and β_2 are the PLEs to describe the dependence of PL on d_1 and d_2, λ_1 and λ_2 are the PLEs to indicate the dependence of PL on θ_t and θ_r, α denotes the intercept parameter associated with the offset value of PL. X_{σ}^{FI} denotes SF, which is modeled as Gaussian distribution $\mathcal{N}(\mu, \sigma^2)$.

$$\begin{aligned} PL_{CI}^{RIS}\left(d_1,d_2,\theta_t,\theta_r\right) =& PL_{FS}^{RIS}(d_0^1, d_0^2, \theta_0^t, \theta_0^r) + 10n_1 \log_{10}\left(\frac{d_1}{d_0^1}\right) + 10n_2 \log_{10}\left(\frac{d_2}{d_0^2}\right) \\ & - 10\mu_1 \log_{10}\left(\frac{\cos\left(\theta_t\right)}{\cos\left(\theta_0^t\right)}\right) - 10\mu_2 \log_{10}\left(\frac{\cos\left(\theta_r\right)}{\cos\left(\theta_0^r\right)}\right) + X_{\sigma}^{CI}, \end{aligned} \tag{13}$$

where n_1 and n_2 are the PLEs to describe the dependence of PL on d_1 and d_2, μ_1 and μ_2 are the PLEs to indicate the dependence of PL on θ_t and θ_r, X_{σ}^{CI} is SF following the Gaussian distribution $\mathcal{N}(\mu, \sigma^2)$, d_0^1, d_0^2, θ_0^t, and θ_0^r denote the reference distances of d_1 and d_2 as well as the reference angles of θ_t and θ_r, respectively. In this paper, d_0^1, d_0^2, θ_0^t, and θ_0^r are set to 1 m, 1 m, 0°, and 0° respectively, whereas these reference values can be adjusted appropriately in each scenario where applicable. Moreover, $PL_{FS}^{RIS}\left(d_0^1, d_0^2, \theta_0^t, \theta_0^r\right)$ represents the PL with these reference variables in free space, which is calculated to be 21.38 dB according to (11). Then, a simplified expression of (13) can be written as

$$\begin{aligned} PL_{CI}^{RIS}\left(d_1,d_2,\theta_t,\theta_r\right) =& 21.38 + 10n_1 \log_{10}\left(d_1\right) + 10n_2 \log_{10}\left(d_2\right) - 10\mu_1 \log_{10}\left(\cos\left(\theta_t\right)\right) \\ & - 10\mu_2 \log_{10}\left(\cos\left(\theta_r\right)\right) + X_{\sigma}^{CI}. \end{aligned} \tag{14}$$

In this paper, the least square (LS) method is utilized to fit the measurement data with the modified FI and CI models, respectively. In detail, LS method adopts Levenberg-marquardt algorithm, which requires presetting the upper and lower bounds of the parameters to be fitted. In this paper, the upper and lower bounds are set to $(50, 3, 3, 2, 2)$ and $(10, 1, 1, 0, 0)$ respectively, for the parameters (α, β_1, β_2, λ_1, λ_2) in the modified FI model. Moreover, the upper and lower bounds are set to $(21.38, 3, 3, 2, 2)$ and $(21.38, 1, 1, 0, 0)$ respectively, for the parameters (PL_{FS}^{RIS}, n_1, n_2, μ_1, μ_2) in the modified CI model.

V. Measurement Results and Modeling Analyses

In this section, the measured channel data in three measurement campaigns is presented and compared with the free-space channel model proposed in [19]. The modified CI and FI models are fitted with the measured channel data under *intelligent reflection with RIS*. Moreover, the channel characteristics in temporal, frequency, and spatial domains including PDP, RMS DS, frequency stationarity, spatial consistency, etc., are analyzed and explained.

A. Outdoor measurement

For the mode of intelligent reflection with RIS in outdoor measurement, the fitting results of the modified CI and FI models with measurement data as well as free-space data are summarized in Table V. From Table V, it can be found that for both of the modified CI and FI models, the fitted PLE on d_1 with free-space data is slightly lower than that with measurement data. On the contrary, the fitted PLE on d_2 with free-space data is slightly higher than that with measurement data. In addition, similar phenomena can be seen in angle domain that the fitted PLEs on θ_t and on θ_r with free-space data are respectively lower and higher than those with measurement data. These phenomena may result from that in outdoor measurement, Rx positions are surrounded by abundant scatterers such as neighbouring buildings while Tx positions are next to open streets.

TABLE V

Fitting results for outdoor measurement.

Parameters	α (PL_{FS}^{RIS})	β_1 (n_1)	β_2 (n_2)	λ_1 (μ_1)	λ_2 (μ_2)
Modified FI with **measurement** data	20.08	2.29	1.88	1.21	0.65
Modified FI with **free-space** data	24.52	2.05	1.95	1.15	0.79
Modified CI with **measurement** data	21.38	2.22	1.82	1.21	0.64
Modified CI with **free-space** data	21.38	2.21	2.08	1.14	0.81

Fig. 8 depicts the modified CI and FI models fitted with the measurement data under $\theta_t = 75^\circ$ and $\theta_r = 60^\circ$. It can be visually observed that both of the proposed models fit well with the measurement data. Fig. 9 exhibits the cumulative distribution functions (CDFs) of SFs for the modified FI and CI models, which are fitted into the Gaussian distributions with a same standard deviation of $\sigma = 2.53$. It delivers a similar prediction accuracy of the modified FI and CI models considering their similar standard deviation.

Fig. 10 provides the measured PL for three modes in outdoor scenario as well as the free-space PL, under $\theta_t = 45^\circ$, $\theta_r = 45^\circ$, and $d_1 = 6$ m. From this figure, the PLE for intelligent reflection mode shows a similar value as the free-space model, though there is a small gap of about 3

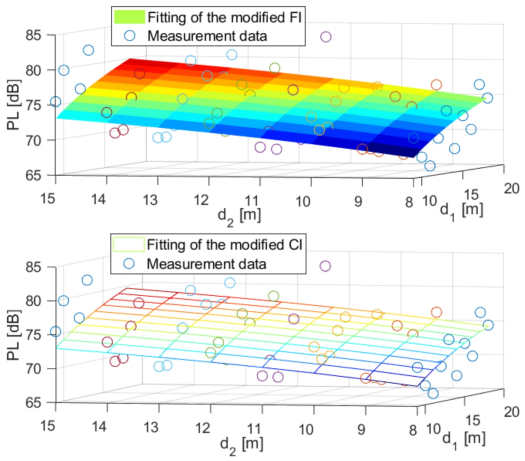


Fig. 8. The modified models with measurement data.

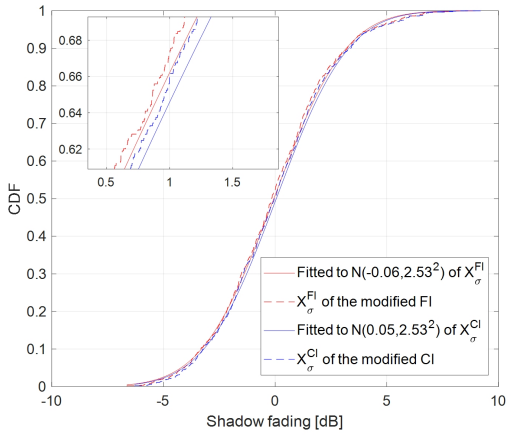


Fig. 9. SFs and the fitted CDFs.

dB between them. In addition, thanks to the capability of focusing signal energy for intelligent reflection mode, its PL demonstrates a maximum gain of 9.7 dB than that for specular reflection mode and a maximum gain of 30 dB than that without RIS, respectively. As d_2 increases, the PL difference between intelligent reflection and specular reflection becomes smaller. When d_2 is large enough, their PLs tend to coincide. This shows that specular reflection and intelligent reflection behave equally in the case of extremely far field, when $\theta_t = \theta_r$. Fig. 11 illustrates the PLs vs EAoA and EAoD under $d_1 = 12 \sim 14$ m and $d_2 = 10 \sim 12$ m for intelligent reflection mode, with color coded against PL. From this figure, the PL keeps up the trend of increasing as EAoA and EAoD become larger, despite a slight fluctuation. This phenomenon is well consistent with the theoretical PL scaling law in angle domain described in [18], [19].

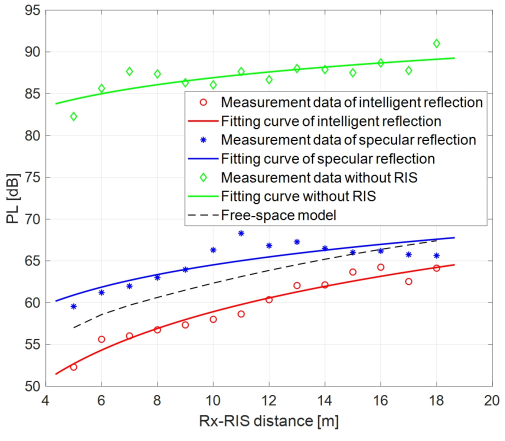


Fig. 10. PLs of measurement data and free-space data.

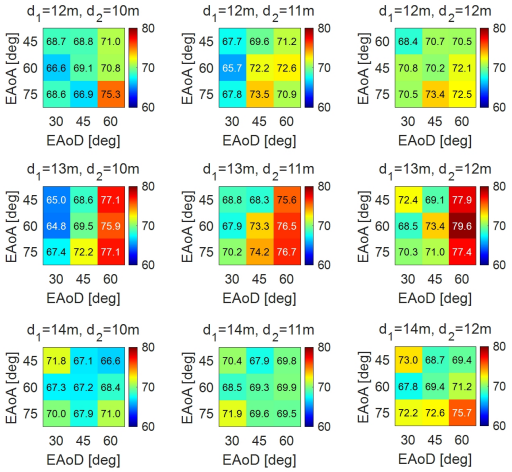


Fig. 11. PLs under $d_1 = 12 \sim 14$ m and $d_2 = 10 \sim 12$ m.

Fig. 12 demonstrates the PDP comparison of three modes under $\theta_t = 45°$, $\theta_r = 45°$, $d_1 = 9$

m, and $d_2 = 8$ m. From this figure, the PDP peak of intelligent reflection mode is highest, followed by that of specular reflection mode, and the PDP peak without RIS is lowest due to its inherent NLOS propagation. Moreover, the delays on PDP peaks of intelligent reflection mode and specular reflection mode are almost the same, which is lower than that without RIS. This can be explained by that the signal propagation without RIS is dominated by the scattering and diffraction aroused from the surroundings, which has a larger excess delay. From field-of-view of Rx, Fig. 13 illustrates the PDP evolution vs d_1 and delay for intelligent reflection mode, which are linked across positions, under $d_2 = 8$ m, $\theta_t = 45°$, $\theta_r = 45°$. It indicates a well stationary spatial consistency on MPC evolution when Tx is moved in our measurement.

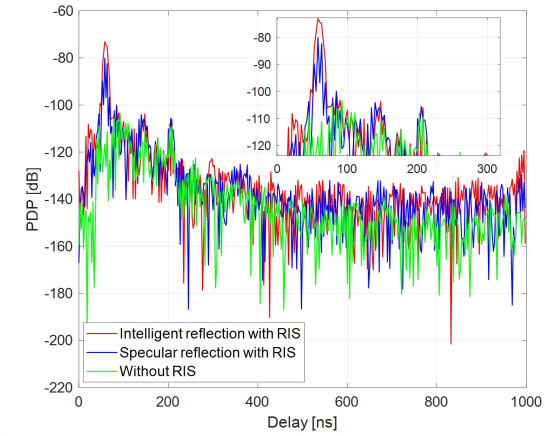


Fig. 12. PDP comparison of three modes.

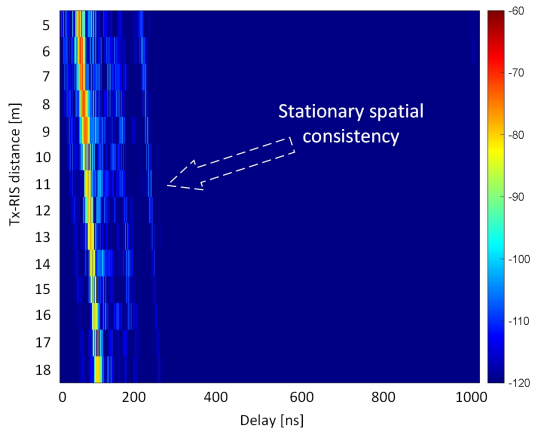


Fig. 13. PDP evolution vs delay and position.

Fig. 14 shows the RMS DSs for three modes and the fitted Gaussian distributions $\mathcal{N}(\mu, \sigma^2)$, under $\theta_t = 45°$ and $\theta_r = 45°$. The means of these CDFs are 8.42 ns, 10.79 ns and 37.55 ns respectively for the modes of intelligent reflection, specular reflection and without RIS, as displayed in Table VI. The higher μ represents the more diffuse multipath distribution. This phenomenon illustrates that the channel time dispersion of intelligent reflection is lower than that of specular reflection, because the latter may cause diffuse reflection of EM waves. In addition, the channel time dispersion without RIS is strongest, on account of that it is dominated by scattering, diffraction, and diffuse reflection.

Fig. 15 demonstrates the frequency stationarity within the measured bandwidth for three modes under $\theta_t = 45°$, $\theta_r = 45°$, $d_1 = 10$ m and $d_2 = 10$ m. From this figure, the propagation signal without RIS shows the strongest frequency selective fading, due to the fact that its dominant propagation originates from rich MPCs. In addition, the propagation signal for specular reflection with RIS demonstrates a slight but non-negligible frequency selective fading, which confirms

TABLE VI

FITTED DISTRIBUTIONS OF RMS DSS.

Scenario	Without RIS		Specular reflection		Intelligent reflection	
	μ [ns]	σ [ns]	μ [ns]	σ [ns]	μ [ns]	σ [ns]
Outdoor	37.55	9.65	10.79	8.79	8.42	6.9
Indoor	13.04	4.29	5.88	4.31	5.01	2.74
O2I	24.21	8.2	16.04	9.69	10.36	9.53

that this mode still generates the additional MPCs when assisting desired signal. By contrast, the intelligent reflection with RIS has a nearly flat signal, illuminating its beamforming capability without creating excrescent MPCs. These phenomena can be numerically explained from their RMS DSs of $\tau^{\mathrm{w}}_{\mathrm{RMS}} = 53.85$ ns, $\tau^{\mathrm{s}}_{\mathrm{RMS}} = 6.94$ ns, and $\tau^{\mathrm{i}}_{\mathrm{RMS}} = 4.95$ ns respectively, considering the signal coherence bandwidth B_c is inversely proportional to its RMS DS, as (15).

$$B_c \propto \frac{1}{\tau_{\mathrm{RMS}}}. \tag{15}$$

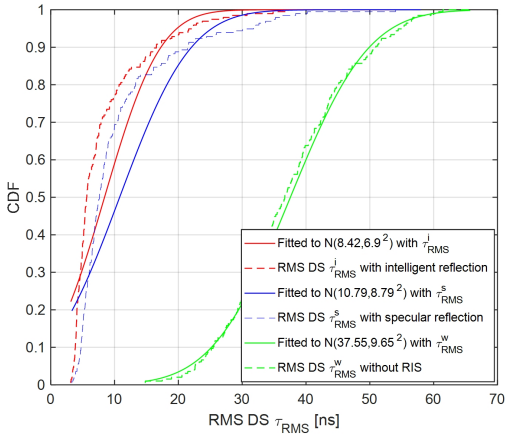


Fig. 14. RMS DSs for three modes.

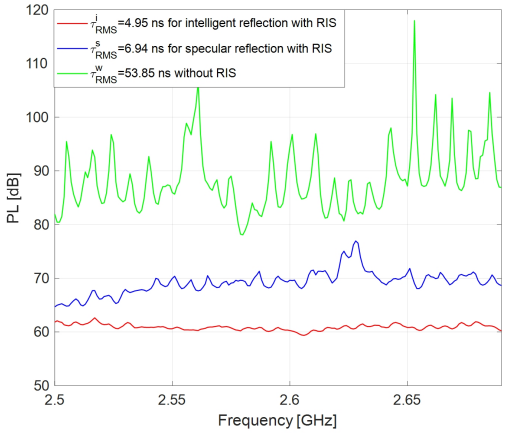


Fig. 15. Frequency stationarity for three modes.

B. *Indoor measurement*

For the mode of intelligent reflection with RIS in indoor measurement, the fitting results of the modified CI and FI models with the measured data as well as the free-space data are summarized in Table VII. Note that in this measurement, the EAoA and EAoD are fixed to be $45°$, thus λ_1 (μ_1) and λ_2 (μ_2) of the modified FI (CI) model are not taken into account. The reference value $PL^{RIS}_{FS} = 26.97$ of the modified CI model is calculated under $\theta_t = 45°$, $\theta_r = 45°$, $d_1 = 1$ m, and $d_2 = 1$ m. From this table, it can be found that for both of the modified CI and FI models, the fitted PLEs on d_1 and d_2 with free-space data are slightly higher than those with measurement

data. This can be explained by that in indoor corridor scenario, there exists a non-ignorable wave-guide effect, which results in the lower PLEs. Fig. 16 exhibits the CDFs of SFs for the modified models, both of which are fitted into the Gaussian distributions with $\sigma = 2.46$. Similar to the outdoor scenario, a similar prediction accuracy between the modified FI and CI models is observed for indoor corridor channels.

Fig. 17 shows the measured PLs for three modes as well as the free-space PL, under $\theta_t = 45°$, $\theta_r = 45°$, and $d_1 = 6$ m. From this figure, the PLE of intelligent reflection mode still shows a approximative value with the free-space PLE, though a small gap of about 4 dB between them is observed. In addition, the PL for intelligent reflection mode demonstrates a maximum gain of 10.6 dB than that for specular reflection mode and a maximum gain of 29.5 dB than that without RIS. Similarly to Fig. 10, as d_2 increases, the PL difference between intelligent reflection and specular reflection get smaller. When d_2 is large enough, their coinciding PLs can be inferred.

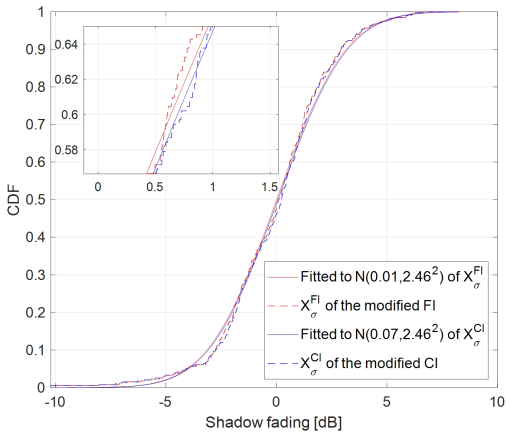


Fig. 16. SFs and the fitted CDFs.

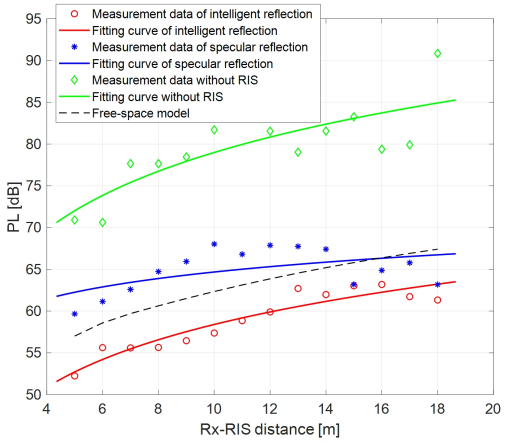


Fig. 17. PLs of measurement data and free-space data.

Fig. 18 illustrates the PDP evolution vs d_1 and delay for three modes respectively, under $d_2 = 8$ m, $\theta_t = 45°$, $\theta_r = 45°$. Firstly, for the intelligent reflection mode, Fig. 18a exhibits a stationary spatial consistency on MPC evolution, despite it shows a small quantity of additional MPCs at 300 ns when d_1 is $5 \sim 13$ m. For the specular reflection mode in Fig. 18b, there are plenty of additional MPCs covering all of the Tx positions. For the mode without RIS, a nonstationary spatial evolution with weak power is observed in Fig. 18c. The above phenomena illustrate that the intelligent reflection mode of RIS is more conducive to focusing signal energy.

Fig. 19 demonstrates the RMS DSs of three modes and the fitted Gaussian distributions $\mathcal{N}(\mu, \sigma^2)$, under $\theta_t = 45°$ and $\theta_r = 45°$. The means of these CDFs are 5.01 ns, 5.88 ns and 13.04 ns for the modes of intelligent reflection, specular reflection and without RIS respectively, as

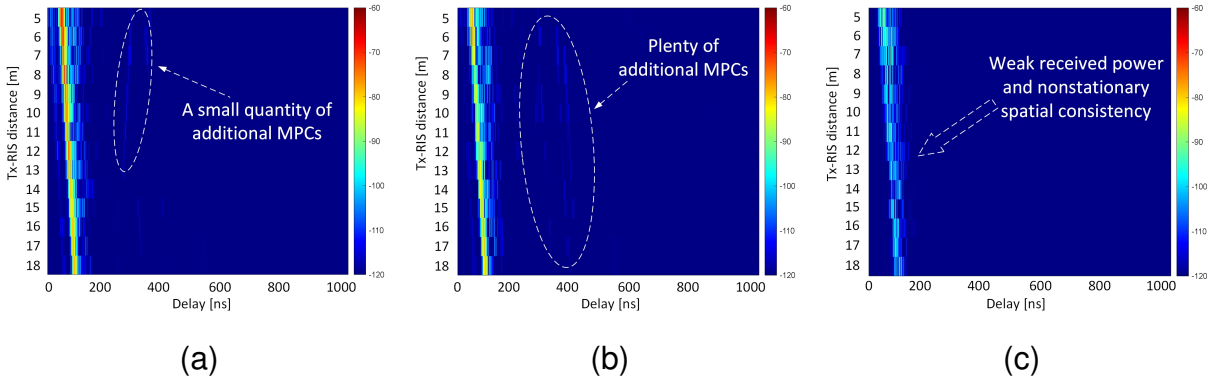


Fig. 18. PDP evolution vs delay and position. (a) Intelligent reflection. (b) Specular reflection. (c) Without RIS.

displayed in Table VI. This phenomenon illustrates that the channel time dispersion of intelligent reflection is lower than that of specular reflection, because of the diffuse reflection of EM waves caused by the latter. The channel time dispersion without RIS is still the strongest, on account of its dominant scattering, diffraction, and diffuse reflection. In addition, it should be noted that these three means in indoor corridor scenario are respectively lower than those (8.42 ns, 10.79 ns and 37.55 ns respectively) in outdoor scenario, which indicates that the signal energy is better focused when in corridor channels.

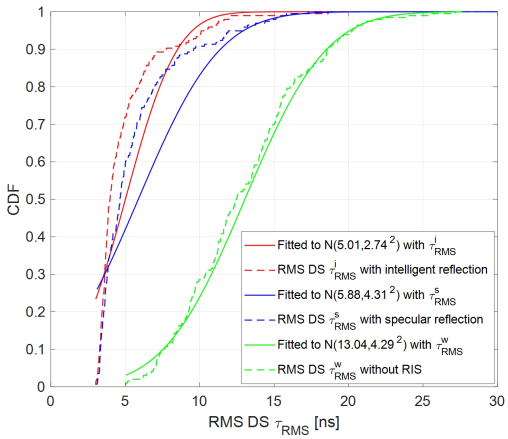


Fig. 19. Comparison of RMS DSs for three modes.

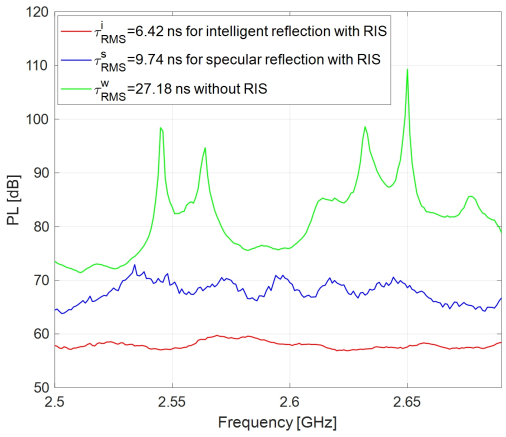


Fig. 20. Frequency stationarity for three modes.

Fig. 20 demonstrates the frequency stationarity within the measured bandwidth for three modes under $\theta_t = 45°$, $\theta_r = 45°$, $d_1 = 8$ m and $d_2 = 8$ m. Similarly to Fig. 15, the propagation signal without RIS shows the strongest frequency selective fading, followed by that of specular reflection with RIS. The intelligent reflection with RIS still has the flattest signal. Their RMS DSs are respectively 27.18 ns, 9.74 ns and 6.42 ns, which accounts for the above phenomena theoretically according to the expression of (15). This phenomenon indicates significantly the

superiority of intelligent beamforming by RIS against "plate metal" or "without RIS", so as to support its claim of "customizing wireless channels".

TABLE VII

FITTING RESULTS FOR INDOOR MEASUREMENT.

Parameters	α (PL_{FS}^{RIS})	β_1 (n_1)	β_2 (n_2)
Modified FI with **measurement** data	28.16	1.9	1.68
Modified FI with **free-space** data	28.7	1.96	1.96
Modified CI with **measurement** data	26.97	1.95	1.74
Modified CI with **free-space** data	26.97	2.04	2.04

TABLE VIII

FITTING RESULTS FOR O2I MEASUREMENT.

Parameters	α (PL_{FS}^{RIS})	β_2 (n_2)
Modified FI with **measurement** data	46.11	1.51
Modified FI with **free-space** data	47.64	1.8
Modified CI with **measurement** data	46.06	1.52
Modified CI with **free-space** data	46.06	2

C. O2I measurement

For the intelligent reflection mode in O2I measurement, the fitting results of the modified CI and FI models with the measured data as well as the free-space data are respectively summarized in Table VIII. Note that only the measured data in left aisle is fitted to the models, where $\theta_t = 45°$, $\theta_r = 45°$, and $d_1 = 9$ m are fixed and the PLE on d_2 is taken into account in Table VIII. The reference value $PL_{FS}^{RIS} = 46.06$ of the modified CI model is calculated under $\theta_t = 45°$, $\theta_r = 45°$, $d_1 = 9$ m, and $d_2 = 1$ m. From this table, we find that for both of the modified CI and FI models, the PLEs on d_2 with free-space data are significantly higher than those with measurement data. This results from that in O2I measurement, there exists plentiful reflection and scattering caused by the surroundings such as desks and chairs. Fig. 21 exhibits the CDFs of SFs for the modified models, both of which are fitted into the Gaussian distributions with $\sigma = 0.48$, indicating their similar and high prediction accuracy.

Fig. 22 shows the RMS DSs of three modes and the fitted Gaussian distributions $\mathcal{N}(\mu, \sigma^2)$. Their means are 10.36 ns, 16.04 ns and 24.21 ns respectively for intelligent reflection, specular reflection and without RIS, as shown in Table VI. The channel time dispersion of intelligent reflection is still the lowest due to its property of focusing energy. Note that these three means in classroom scenario are higher than those (8.42 ns, 10.79 ns and 37.55 ns respectively) in outdoor scenario and those (5.01 ns, 5.88 ns and 13.04 ns respectively) in corridor scenario. This indicates that the time dispersion for RIS-assisted channel in O2I scenario is strongest.

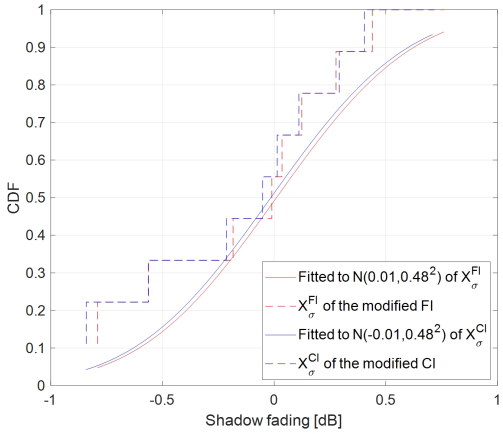


Fig. 21. SFs and the fitted CDFs in left aisle.

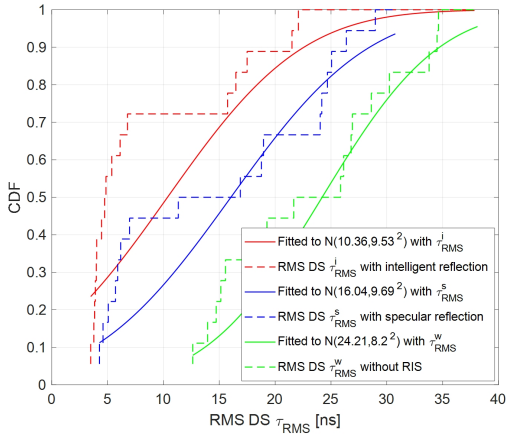


Fig. 22. Comparison of RMS DSs for three modes.

Fig. 23 shows the measured PLs for three modes in left and right aisles respectively as well as the free-space PLs. Note that in right aisle, the Positions 1 and 2 are discarded because their propagation links with RIS are blocked by the teacher's table during the measurement. In left aisle shown in Fig. 23a, the PLE on d_2 of intelligent reflection mode is slightly lower than that of free-space PLE, resulting from the abundant scatters in this classroom. In addition, the PL for intelligent reflection demonstrates an improvement of about 7 dB than that for specular reflection and an improvement of about $25 \sim 30$ dB than that without RIS. From Fig. 23b, the PLE on d_2 of intelligent reflection mode is greatly lower than that of free-space PLE in right aisle. The PL for intelligent reflection mode demonstrates an improvement of about $15 \sim 20$ dB than that with specular reflection mode and an improvement of about $20 \sim 25$ dB than that without RIS.

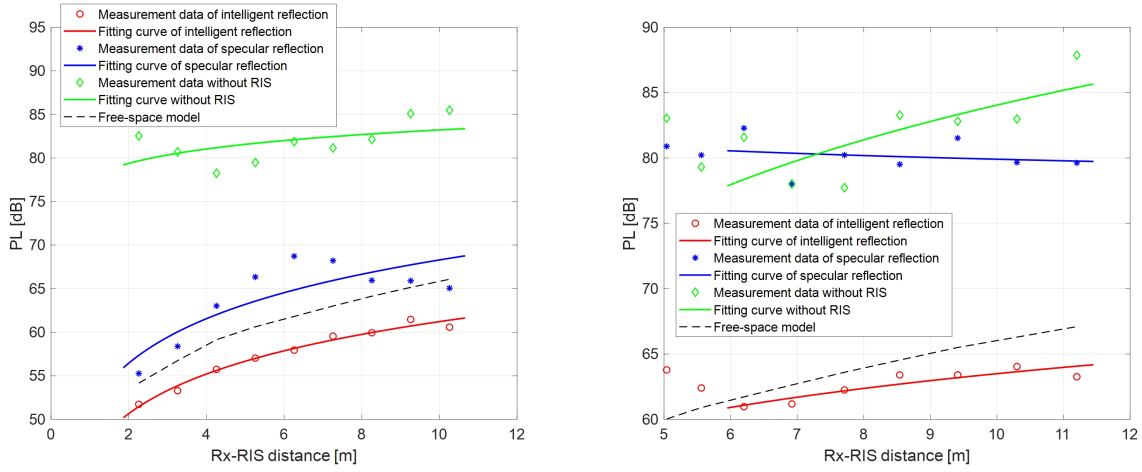


Fig. 23. PL comparison of measurement data and free-space data. (a) In left aisle. (b) In right aisle.

Fig. 24 demonstrates the frequency stationarity within the measured bandwidth for three modes

at Position 5 in left and right aisles, respectively. From Fig. 24a, in left aisle, the RMS DSs are $\tau^{\mathrm{i}}_{\mathrm{RMS}} = 3.99$ ns, $\tau^{\mathrm{s}}_{\mathrm{RMS}} = 16.89$ ns and $\tau^{\mathrm{w}}_{\mathrm{RMS}} = 19.27$ ns respectively for the modes of intelligent reflection, specular reflection as well as without RIS. Their signals are respectively flat, slight frequency selective fading, and strong frequency selective fading. As shown in Fig. 24b, in right aisle, the frequency stationarity for the modes of intelligent reflection and without RIS are similar to those in Fig. 24a. Nevertheless, the specular reflection mode in this figure illustrates a stronger frequency selective fading than that in left aisle. This attributes to that the specular reflection mode is incapable of covering the Rx positions in right aisle directly, where only the reflected and scattered signals arrive at Rx.

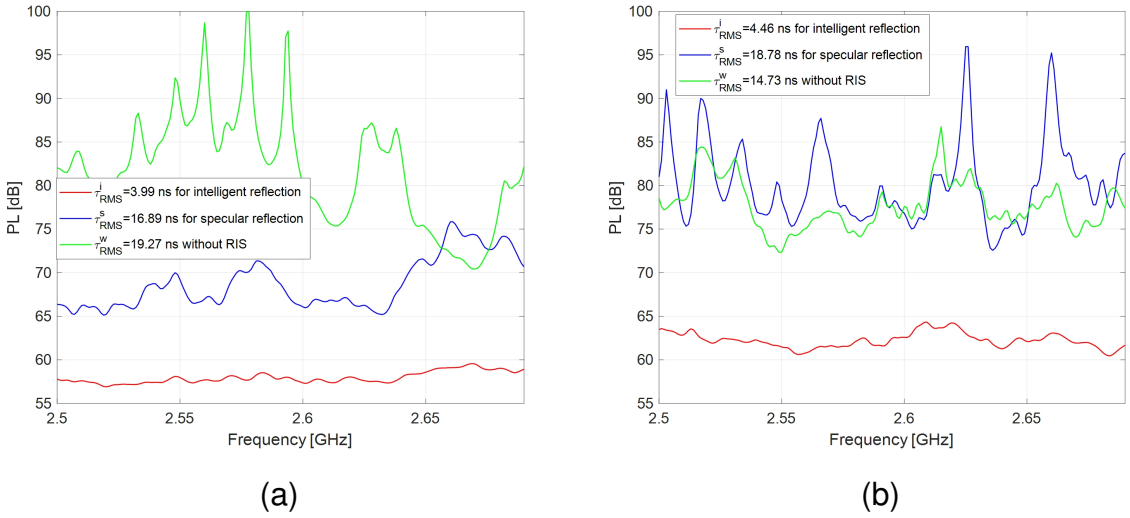


Fig. 24. Frequency stationarity for three modes. (a) In left aisle. (b) In right aisle.

D. Summary of measurement and modeling

1) Channel measurement

On **PL**: In indoor and outdoor measurement, the PLEs on both distance and angle for intelligent reflection mode are approximate to the free-space PLEs. In O2I measurement, the PLE with the measured data is prominently lower than that in free space, which may result from the abundant scattering in classroom. In addition, a slight gap between the measured PL and free-space PL is observed. In all of the three measurements, the intelligent reflection with RIS shows a significant improvement on PL covering multiple desired directions, against that of specular reflection mode as well as the mode without RIS.

On **RMS DS**: For intelligent reflection with RIS, specular reflection with RIS, and the mode without RIS, their means of RMS DSs are respectively 10.36 ns, 16.04 ns and 24.21 ns in O2I

scenario, 8.42 ns, 10.79 ns and 37.55 ns in outdoor scenario, as well as 5.01 ns, 5.88 ns and 13.04 ns in indoor scenario. This indicates that for RIS-assisted channel, the time dispersion is the strongest in O2I scenario, followed by outdoor scenario, and the weakest time dispersion occurs in indoor channel. Moreover, the intelligent reflection is evidently favorable for focusing signal energy and reducing time dispersion.

On **frequency stationarity**: In all of the three measurements, the intelligent reflection with RIS demonstrates a flat propagation signal. By contrast, the specular reflection with RIS shows a slight but non-negligible frequency selective fading and the propagation mode without RIS manifests the strongest frequency selective fading. These phenomena evidence that the intelligent reflection with RIS is advantageous for enhancing frequency stationarity and may pave the way for promoting RIS-empowered high data rate transmission.

On **spatial consistency**: The MPC evolution for intelligent reflection mode shows a stationary spatial consistency as the variation of distance. In addition, plenty of additional MPCs are observed for specular reflection mode. For the mode without RIS, a nonstationary spatial consistency with weak power is detected. This may have implications on the future research such as RIS-empowered beam tracking.

2) Channel modeling

On **modeling accuracy**: Both of the the modified FI and CI models can be viewed as accurate and generalizable models to predict the PL characteristics of RIS-assisted channel covering distance and angle domains. Their fitting standard deviations are 2.53 dB in outdoor scenario, 2.46 dB in indoor scenario, as well as 0.48 dB in O2I scenario. This phenomenon illustrates that for RIS-assisted channel, the proposed two models show a similar and high prediction accuracy. These results may has the instructive significance for future RIS-related PL evolution as well as modeling standardization.

On **modeling complexity**: The proposed two empirical models are inherited from the traditional FI and CI models respectively, which have been widely considered in reports, specifications and studies. The modified FI and CI models only parameterize several variables with the formal expression unchanged, while more comprehensively predicting the propagation characteristics for RIS-assisted channel. Thus, the modeling complexity can be reasonably acceptable and widely applicable for RIS-related practical deployment in the future.

VI. Conclusions

In this paper, we conducted multi-scenario broadband channel measurement campaigns and channel modeling for RIS-assisted SISO channel at 2.6 GHz. Utilizing the VNA-based measurement system and a fabricated RIS, three measurements including outdoor, indoor and O2I scenarios were carried out, with 2096 channel acquisitions collected. In each scenario, three propagation modes including intelligent reflection with RIS, specular reflection with RIS, and the mode without RIS were measured. In addition, two modified empirical models including FI and CI, were proposed to cater for the cascaded characteristics of RIS-assisted channel. From the measurement results, the PL for "intelligent reflection with RIS" is significantly lower than that for "specular reflection with RIS" and that for "without RIS", which manifests its potential of improving the channel quality. The PLEs in outdoor and indoor scenarios show similar values as those in free space. Nevertheless, the PLE in O2I scenario is prominently lower than the free space value, which may be due to the plentiful scattering and reflection of the surroundings. Furthermore, for RIS-assisted channel, RMS DSs are highest in O2I scenario, followed by outdoor scenario, and the RMS DSs in indoor scenario are lowest. From the perspective of propagation mode, the intelligent reflection is more favorable for focusing signal energy and reducing time dispersion. Additionally, the measurement results also illustrate that the intelligent reflection with RIS is beneficial to enhancing frequency stationarity. The MPC evolution for intelligent reflection mode shows a more stationary spatial consistency. In our future studies, more diverse yet typical RIS-assisted communication scenarios such as urban macro cell (UMa) and MIMO, will be further measured and verified.

References

[1] M. W. Akhtar, S. A. Hassan, R. Ghaffar, H. Jung, S. Garg, and M. S. Hossain, "The shift to 6G communications: vision and requirements," *Hum. Cent. Comput. Inf. Sci.*, vol.10, no. 53, Dec. 2020.

[2] F. Tariq, M. R. A. Khandaker, K.-K. Wong, M. A. Imran, M. Bennis, and M. Debbah, "A Speculative Study on 6G," *IEEE Wireless Commun.*, vol. 27, no. 4, pp. 118-125, Aug. 2020.

[3] M. Giordani, M. Polese, M. Mezzavilla, S. Rangan, and M. Zorzi, "Toward 6G Networks: Use Cases and Technologies," *IEEE Commun. Mag.*, vol. 58, no. 3, pp. 55-61, Mar. 2020.

[4] C.-X. Wang, J. Huang, H. Wang, X. Gao, X. You, and Y. Hao, "6G Wireless Channel Measurements and Models: Trends and Challenges," *IEEE Veh. Technol. Mag.*, vol. 15, no. 4, pp. 22-32, Dec. 2020.

[5] H. Tataria, M. Shafi, M. Dohler, and S. Sun, "Six Critical Challenges for 6G Wireless Systems: A Summary and Some Solutions," *IEEE Veh. Technol. Mag.*, vol. 17, no. 1, pp. 16-26, Mar. 2022.

[6] S. Basharat, S. A. Hassan, H. Pervaiz, A. Mahmood, Z. Ding, and M. Gidlund, "Reconfigurable Intelligent Surfaces: Potentials, Applications, and Challenges for 6G Wireless Networks," *IEEE Wireless Commun.*, vol. 28, no. 6, pp. 184-191, Dec. 2021.

[7] E. C. Strinati, G. C. Alexandropoulos, H. Wymeersch, B. Denis, V. Sciancalepore, R. D'Errico, A. Clemente, D. Phan-Huy, E. De Carvalho, and P. Popovski, "Reconfigurable, Intelligent, and Sustainable Wireless Environments for 6G Smart Connectivity," *IEEE Commun. Mag.*, vol. 59, no. 10, pp. 99-105, Oct. 2021.

[8] K. Feng, X. Li, Y. Han, and Y.-J. Chen, "Joint Beamforming Optimization for Reconfigurable Intelligent Surface-Enabled MISO-OFDM Systems," *China Commun.*, vol. 18, no. 3, pp. 63-79, Mar. 2021.

[9] T. J. Cui, M. Q. Qi, X. Wan, J. Zhao, and Q. Cheng, "Coding metamaterials, digital metamaterials and programmable metamaterials," *Light-Sci. Appl.*, vol. 3, pp. 1-9, Oct. 2014.

[10] M. Di Renzo, A. Zappone, M. Debbah, M.-S. Alouini, C. Yuen, J. de Rosny, and S. Tretyakov, "Smart Radio Environments Empowered by Reconfigurable Intelligent Surfaces: How It Works, State of Research, and the Road Ahead," *IEEE J. Sel. Areas Commun.*, vol. 38, no. 11, pp. 2450-2525, Nov. 2020.

[11] Q. Wu and R. Zhang, "Towards Smart and Reconfigurable Environment: Intelligent Reflecting Surface Aided Wireless Network," *IEEE Commun. Mag.*, vol. 58, no. 1, pp. 106-112, Jan. 2020.

[12] Y. Lin, S. Jin, M. Matthaiou, and X. You, "Channel Estimation and User Localization for IRS-Assisted MIMO-OFDM Systems," *IEEE Trans. Wireless Commun.*, vol. 21, no. 4, pp. 2320-2335, Apr. 2022.

[13] K. Feng, X. Li, Y. Han, S. Jin, and Y. Chen, "Physical Layer Security Enhancement Exploiting Intelligent Reflecting Surface," *IEEE Commun. Lett.*, vol. 25, no. 3, pp. 734-738, Mar. 2021.

[14] K. Feng, Q. Wang, X. Li, and C.-K. Wen, "Deep Reinforcement Learning Based Intelligent Reflecting Surface Optimization for MISO Communication Systems," *IEEE Wireless Commun. Lett.*, vol. 9, no. 5, pp. 745-749, May 2020.

[15] L. Jiang, X. Li, M. Matthaiou, and S. Jin, "Joint User Scheduling and Phase Shift Design for RIS Assisted Multi-cell MISO Systems," *IEEE Wireless Commun. Lett.*, vol. 12, no. 3, pp. 431-435, Mar. 2023.

[16] J. Sang, Y. Yuan, W. Tang, Y. Li, X. Li, S. Jin, Q. Cheng, and T. J. Cui, "Coverage Enhancement by Deploying RIS in 5G Commercial Mobile Networks: Field Trials," *IEEE Wireless Commun.*, early access, Dec. 2022.

[17] J. Huang, C.-X. Wang, Y. Sun, R. Feng, J. Huang, B. Guo, Z. Zhong, and T. J. Cui, "Reconfigurable Intelligent Surfaces: Channel Characterization and Modeling," *Proc. IEEE*, vol. 110, no. 9, pp. 1290-1311, Sept. 2022.

[18] W. Tang, M. Z. Chen, X. Chen, J. Y. Dai, Y. Han, M. Di Renzo, Y. Zeng, S. Jin, Q. Cheng, and T. J. Cui, "Wireless Communications with Reconfigurable Intelligent Surface: Path Loss Modeling and Experimental Measurement," *IEEE Trans. Wireless Commun.*, vol. 20, no. 1, pp. 421-439, Jan. 2021.

[19] W. Tang, X. Chen, M. Z. Chen, J. Y. Dai, Y. Han, M. Di Renzo, S. Jin, Q. Cheng, and T. J. Cui, "Path Loss Modeling and Measurements for Reconfigurable Intelligent Surfaces in the Millimeter-Wave Frequency Band," *IEEE Trans. Commun.*, vol. 70, no. 9, pp. 6259-6276, Sept. 2022.

[20] R. Zhou, X. Chen, W. Tang, X. Li, S. Jin, E. Basar, Q. Cheng, and T. J. Cui, "Modeling and Measurements for Multi-path Mitigation with Reconfigurable Intelligent Surfaces," in *Proc. IEEE EuCAP*, Madrid, Spain, pp. 1-5. Mar. 2022.

[21] S. W. Ellingson, "Path loss in reconfigurable intelligent surface-enabled channels," in *Proc. IEEE PIMRC*, Helsinki, Finland, pp. 829–835. Sept. 2021.

[22] J. C. B. Garcia, A. Sibille, and M. Kamoun, "Reconfigurable intelligent surfaces: Bridging the gap between scattering and reflection," *IEEE J. Sel. Areas Commun.*, vol. 38, no. 11, pp. 2538–2547, Nov. 2020.

[23] F. H. Danufane, M. D. Renzo, J. de Rosny, and S. Tretyakov, "On the path-loss of reconfigurable intelligent surfaces: An approach based on Green's theorem applied to vector fields," *IEEE Trans. Commun.*, vol. 69, no. 8, pp. 5573–5592, Aug. 2021.

[24] O. Ozdogan, E. Bjornson, and E. G. Larsson, "Intelligent reflecting surfaces: Physics, propagation, and pathloss modeling," *IEEE Wireless Commun. Lett.*, vol. 9, no. 5, pp. 581–585, May 2020.

[25] M. Najafi, V. Jamali, R. Schober, and H. V. Poor, "Physics-based modeling and scalable optimization of large intelligent reflecting surfaces," *IEEE Trans. Commun.*, vol. 69, no. 4, pp. 2673–2691, Apr. 2021

[26] E. Basar and I. Yildirim, "Reconfigurable Intelligent Surfaces for Future Wireless Networks: A Channel Modeling Perspective," *IEEE Wireless Commun.*, vol. 28, no. 3, pp. 108-114, Jun. 2021.

[27] W. Tang, X. Chen, M. Z. Chen, J. Y. Dai, Y. Han, S. Jin, Q. Cheng, G. Ye Li, and T. J. Cui, "On Channel Reciprocity in Reconfigurable Intelligent Surface Assisted Wireless Networks," *IEEE Wireless Commun.*, vol. 28, no. 6, pp. 94-101, Dec. 2021.

[28] G. C. Trichopoulos, P. Theofanopoulos, B. Kashyap, A. Shekhawat, A. Modi, T. Osman, S. Kumar, A. Sengar, A. Chang, and A. Alkhateeb, "Design and Evaluation of Reconfigurable Intelligent Surfaces in Real-World Environment," *IEEE Open J. Commun. Soc.*, vol. 3, pp. 462-474, 2022.

[29] X. Pei, H. Yin, L. Tan, L. Cao, Z. Li, K. Wang, K. Zhang, and E. Björnson, "RIS-Aided Wireless Communications: Prototyping, Adaptive Beamforming, and Indoor/Outdoor Field Trials," *IEEE Trans. Commun.*, vol. 69, no. 12, pp. 8627-8640, Dec. 2021.

[30] X. Tan, Z. Sun, J. M. Jornet, and D. Pados, "Increasing Indoor Spectrum Sharing Capacity Using Smart Reflect-array," in *Proc. IEEE ICC*, Kuala Lumpur, Malaysia, pp. 1-6. May 2016.

[31] A. Araghi, M. Khalily, M. Safaei, A. Bagheri, V. Singh, F. Wang, and R. Tafazolli, "Reconfigurable Intelligent Surface (RIS) in the Sub-6 GHz Band: Design, Implementation, and Real-World Demonstration," *IEEE Access*, vol. 10, pp. 2646-2655, Jan. 2022.

[32] J. Rains, J. R. Kazim, A. Tukmanov, T. J. Cui, L. Zhang, Q. H. Abbasi, and M. A. Imran, "High-Resolution Programmable Scattering for Wireless Coverage Enhancement: An Indoor Field Trial Campaign," *IEEE Trans. Antennas Propag.*, vol. 71, no. 1, pp. 518-530, Jan. 2023.

[33] J.-B. Gros, V. Popov, M. A. Odit, V. Lenets, and G. Lerosey, "A Reconfigurable Intelligent Surface at mmWave Based on A Binary Phase Tunable Metasurface," *IEEE Open J. Commun. Soc.*, vol. 2, pp. 1055-1064, 2021.

[34] A. Mudonhi, M. Lotti, A. Clemente, R. D' Errico, and C. Oestges, "RIS-enabled mmWave channel sounding based on electronically reconfigurable transmitarrays," in *Proc. IEEE EuCAP*, Dusseldorf, Germany, pp. 1–5. Mar. 2021.

[35] S. Kayraklık, I. Yildirim, Y. Gevez, E. Basar, and A. Görçin, "Indoor Coverage Enhancement for RIS-Assisted Communication Systems: Practical Measurements and Efficient Grouping," [Online]. Available: https://arxiv.org/abs/2211.07188.

[36] S. Keşir, S. Kayraklık, İ. Hökelek, A. E. Pusane, E. Basar, and Ali Görçin, "Measurement-based Characterization of Physical Layer Security for RIS-assisted Wireless Systems," [Online]. Available: https://arxiv.org/abs/2212.07254.

[37] 3GPP, "Base Station (BS) radio transmission and reception", 3GPP Tech. Spec., 38.104 (V16.13.0), Sept. 2022.

[38] B. Gao, J. Li, Z. Yu, J. Sang, M. Zhou, J. Lan, W. Tang, X. Li, and S. Jin, "Propagation Characteristics of RIS-assisted Wireless Channels in Corridors: Measurements and Analysis," in *Proc. IEEE/CIC*, Foshan, China, pp. 550-554. Aug. 2022.

[39] J. Sang, J. Lan, M. Zhou, B. Gao, W. Tang, X. Li, X. Yi, and S. Jin, "Quantized Phase Alignment by Discrete Phase Shifts for Reconfigurable Intelligent Surface-Assisted Communication Systems," [Online]. Available: https://arxiv.org/abs/2303.13046.

[40] P. Zhang, B. Yang, C. Yi, H. Wang, and X. You, "Measurement-Based 5G Millimeter-Wave Propagation Characterization in Vegetated Suburban Macrocell Environments," *IEEE Trans. Antennas Propag.*, vol. 68, no. 7, pp. 5556-5567, Jul. 2020.

[41] 3GPP, "Study on channel model for frequency from 0.5 to 100 GHz", 3GPP Tech. Rep., 38.901 (V16.1.0), Dec. 2019.

[42] ITU-R, "Multipath Propagation and Parameterization of its Characteristics", ITU-R Tech. Rep., P. 1407-6, 2017.